Supporting Information

Porous Organic Polymers Incorporating BODIPY Moieties for Efficient Removal of Organic Dyes from Aqueous Solutions

Lihua Guo, Qiming Huo, Shengyu Feng, Dengxu Wang, Hongzhi Liu*

National Engineering Research Center for Colloidal Materials & Key Laboratory of Special Functional Aggregated Materials, Ministry of Education, Shandong Key Laboratory of Advanced Organosilicon Materials and Technologies, School of Chemistry and Chemical Engineering, Shandong University, Jinan 250100, P. R. China

*Corresponding author's e-mail: dxwang@sdu.edu.cn

Table of contents

Characterization.

Fig. S1. Standard working curves for rhodamine B (a), congo red (b), methylene blue (c), and methyl orange (d)

Fig. S2. (a) FT-IR spectroscopy of BIPOP-1, M-1 and M-2, (b) FT-IR spectroscopy of BIPOP-1 indicating the presence of C≡C

Fig. S3. (a) FT-IR spectroscopy of BIPOP-2, M-1 and M-3, (b) FT-IR spectroscopy of BIPOP-2 indicating the presence of C≡C

Fig. S4. ^{13}C NMR of M-1 and M-2. The pound signs denote the solvents

Fig. S5. (a) XRD spectra of BIPOPs. The peaks at 2θ ≈ 22° are derived from Si-O-Si linkages in test glass device. (b) TGA curve of BIPOPs. (c-d) Scanning electron microscopy (SEM) images of BIPOP-1 (c) and BIPOP-2 (d)

Fig. S6. Equilibrium adsorption isotherms of BIPOP-2 towards various dyes

Fig. S7. Equilibrium adsorption isotherms of BIPOP-1 towards RB with error bars based on triplicate measurement

Fig. S8. The adsorption kinetics of BIPOP-1 towards RB. (a) Kinetic equilibrium curve

of RB onto BIPOP-1 with an initial concentration of 50 mg/L with the error bars based on triplicate measurements. (b) The time-dependent UV-vis spectra along with time plot; (c) The removal efficiency (%) vs time plot.

Fig. S9. Equilibrium adsorption isotherms of CPOP towards various dyes

Fig. S10. FT-IR spectroscopy of BIPOP-1, RB and RB-loaded BIPOP-1

Fig. S11. Wide-scan XPS spectra of BIPOP-1 and RB-loaded BIPOP-1

Fig. S12. High resolution XPS spectra of N1s

Fig. S13. (a) ^{13}C NMR spectra of RB, and BODIPY-2H, and their mixture; (b) ^{19}F NMR spectra of BODIPY-2H and its mixture with RB

Fig. S14. The ^{11}B NMR spectra of BODIPY-2H and its mixture with RB

Fig. S15. The FT-IR spectroscopy of the pristine and recycled BIPOP-1

Fig. S16. The FE-SEM images of the pristine and recycled BIPOP-1

Fig. S17. BET plots of BIPOP-1 (r = 0.999982, C = 118.639)

Fig. S18. BET plots of BIPOP-2 (r = 0.999947, C = 378.787)

Fig. S19. BET plots of CPOP (r = 0.999977, C = 325.499)

Table S1. Comparison of the adsorption capacities of BIPOPs towards MO with other adsorbents

Table S2. Comparison of the adsorption capacity of BIPOPs on CR with other adsorbents

Table S3. Comparison of the adsorption capacity of BIPOPs on MB with other adsorbents

Table S4. Size and molecular properties of dye molecules

Table S5. The comparison of equilibrium adsorption capacities (Q_e) of RB adsorbed by BIPOP-1 in pure water and seawater from Bohai sea

Table S6. Electronic binding energy of various elements in BIPOP-1, RB, and RB-

loaded BIPOP-1

References

Characterization. Fourier transform infrared (FT-IR) spectra were measured within a 4000 to 400 cm^{-1} region on a Bruker TENSOR-27 infrared spectrophotometer (KBr pellet). ^{1}H NMR, ^{13}C NMR, ^{19}F NMR, and ^{11}B NMR spectra were measured on a Bruker AVANCE-300 or 400 NMR spectrometer. Solid-state ^{13}C and ^{29}Si cross-polarization/magic-angle-spinning (CP/MAS) NMR spectra were recorded on a Bruker AVANCE-500 NMR spectrometer operating at a magnetic field strength of 9.4 T. The resonance frequencies at this field strength were 125 and 99 MHz for ^{13}C and ^{29}Si NMR, respectively. A chemagnetics 5 mm triple-resonance MAS probe was used to acquire ^{13}C and ^{29}Si NMR spectra. ^{29}Si MAS NMR spectra with high power proton decoupling were recorded by using a p/2 pulse length of 5 ms, a recycle delay of 120 s, and a spinning rate of 5 kHz. Elemental analyses were conducted using an Elementar vario EL III elemental analyzer.

Thermogravimetric analysis (TGA) was conducted under N_2 using a TA SDTQ600 at a temperature range of room temperature to 800°C with a heating rate of 10 °C min^{-1}. Field-emission scanning electron microscopy (FE-SEM) experiments were determined by using HITACHI S4800 Spectrometer. Powder X-ray diffraction (PXRD) were carried out on a Riguku D/MAX 2550 diffractometer with Cu-Kα radiation, 40 kV, 20 mA with the 2θ range of 10°~90° (scanning rate of 10° min^{-1}) at room temperature. Nitrogen sorption isotherm measurements were performed using a Micro meristics surface area and a pore size analyzer. Before measurement, the samples were degassed at 100°C for at least 12 h. A sample of ca. 100 mg and a UHP-grade nitrogen (99.999%) gas source were used for the nitrogen sorption measurements conducted at 77K and

collected on a Quantachrome Quadrasorb apparatus. Brunauer-Emmett-Teller (BET) surface areas were determined over a P/P_0 range from 0.01 to 0.20. Nonlocal density functional theory (NLDFT) pore size distributions were determined using the carbon/slit cylindrical pore mode of the Quadrawin software. X-ray photoelectron spectroscopy (XPS) was conducted on a Thermo Fischer ESCALAB 250Xi using a monochromatic Al Kα (1486.8 eV) X-ray source with a spot size of 500 μm. The anode was operated at 12.5 kV and 16 mA. Ultraviolet absorption (UV) spectra were performed with TU-1901 double UV–Vis spectrophotometer.

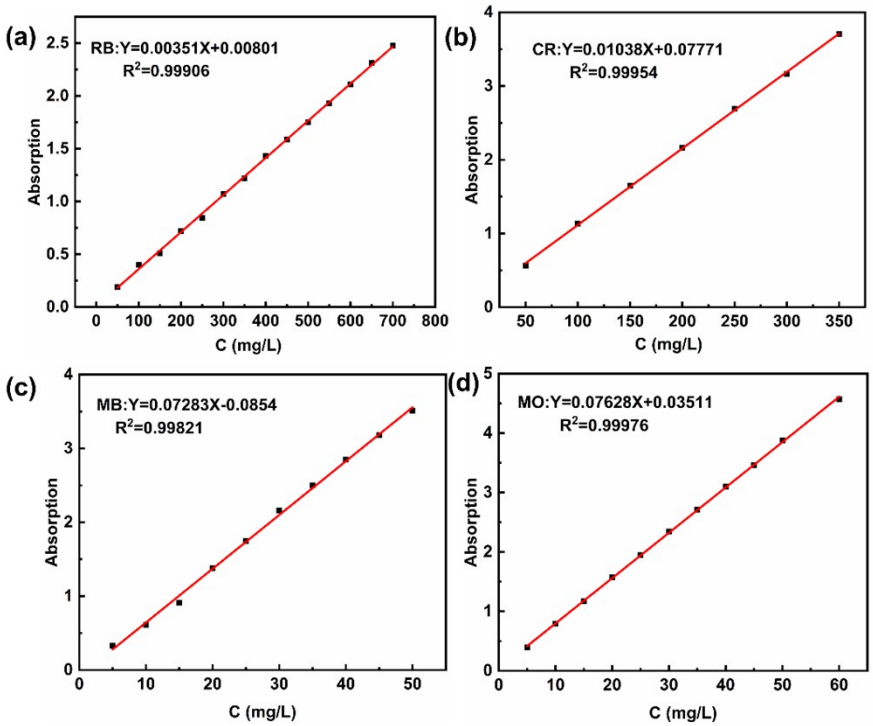

Fig. S1. Standard working curves for rhodamine B (a), congo red (b), methylene blue (c), and methyl orange (d)

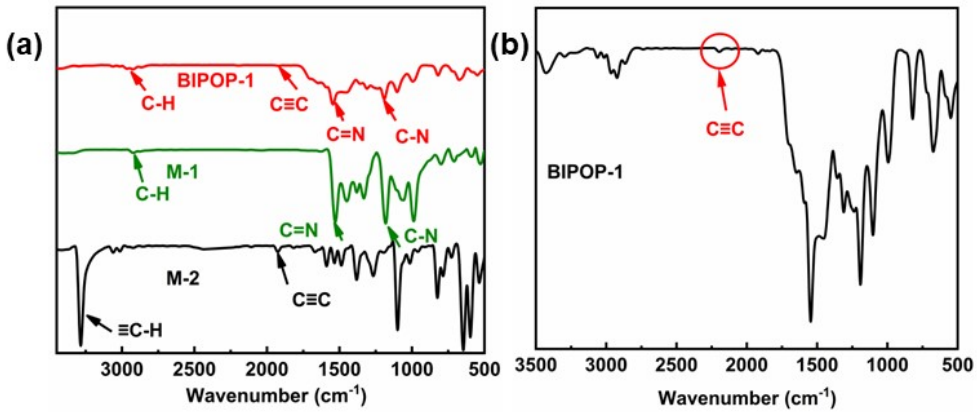

Fig. S2. (a) FT-IR spectroscopy of BIPOP-1, M-1 and M-2, (b) FT-IR spectroscopy of BIPOP-1 indicating the presence of C≡C

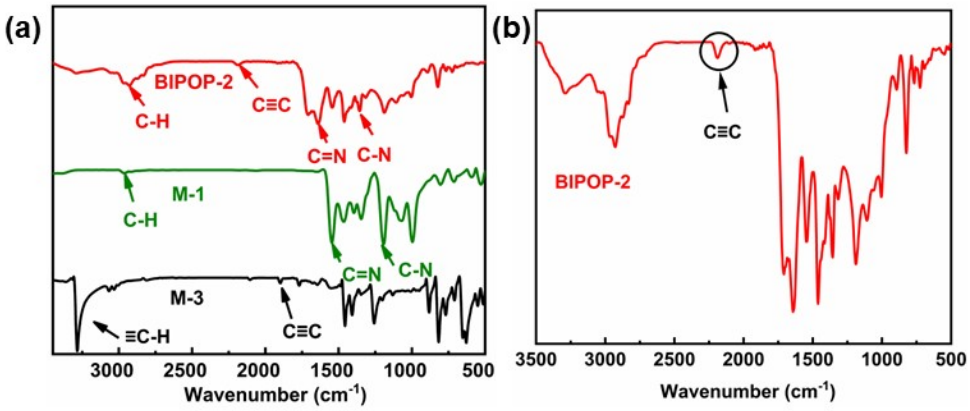

Fig. S3. (a) FT-IR spectroscopy of BIPOP-2, M-1 and M-3, (b) FT-IR spectroscopy of BIPOP-2 indicating the presence of C≡C

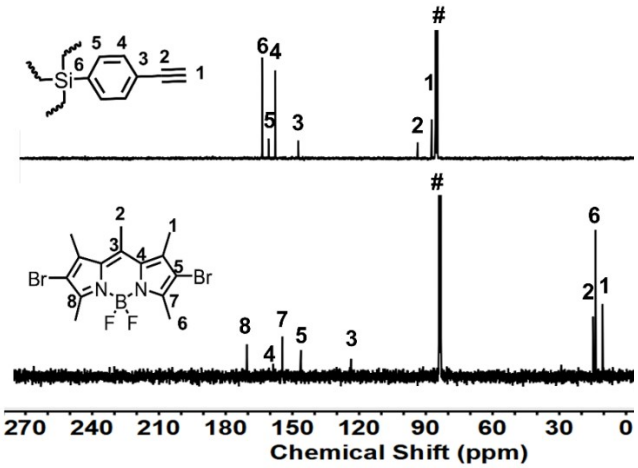

Fig. S4. ^{13}C NMR of M-1 and M-2. The pound signs denote the solvents.

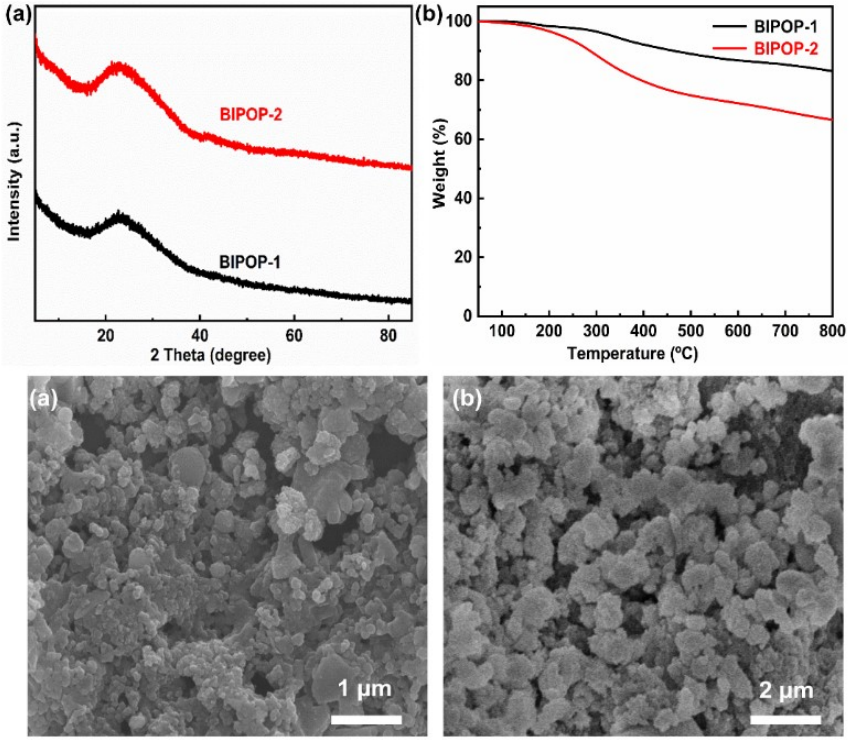

Fig. S5. (a) XRD spectra of BIPOPs. The peaks at 2θ ≈ 22° are derived from Si-O-Si linkages in test glass device. (b) TGA curve of BIPOPs. (c-d) Scanning electron microscopy (SEM) images of BIPOP-1 (c) and BIPOP-2 (d)

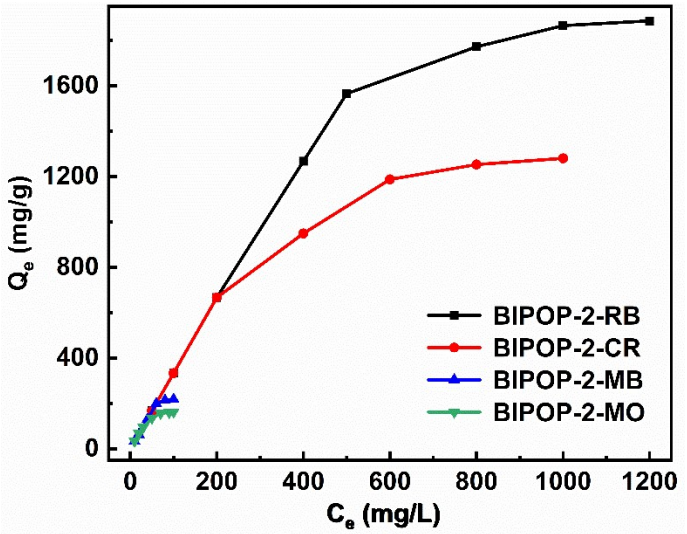

Fig. S6. Equilibrium adsorption isotherms of BIPOP-2 towards various dyes

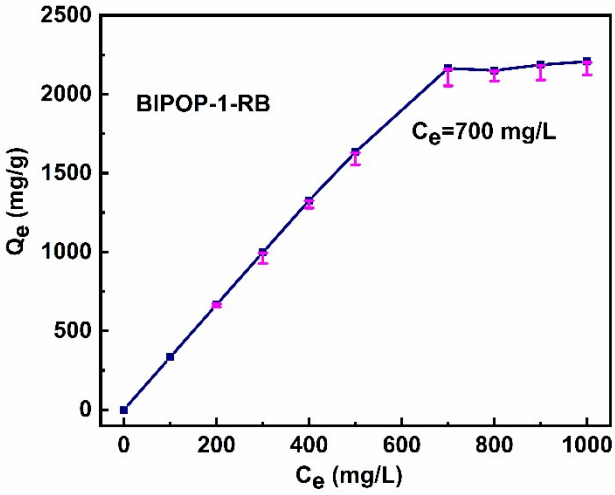

Fig. S7. Equilibrium adsorption isotherms of BIPOP-1 towards RB with error bars based on triplicate measurement

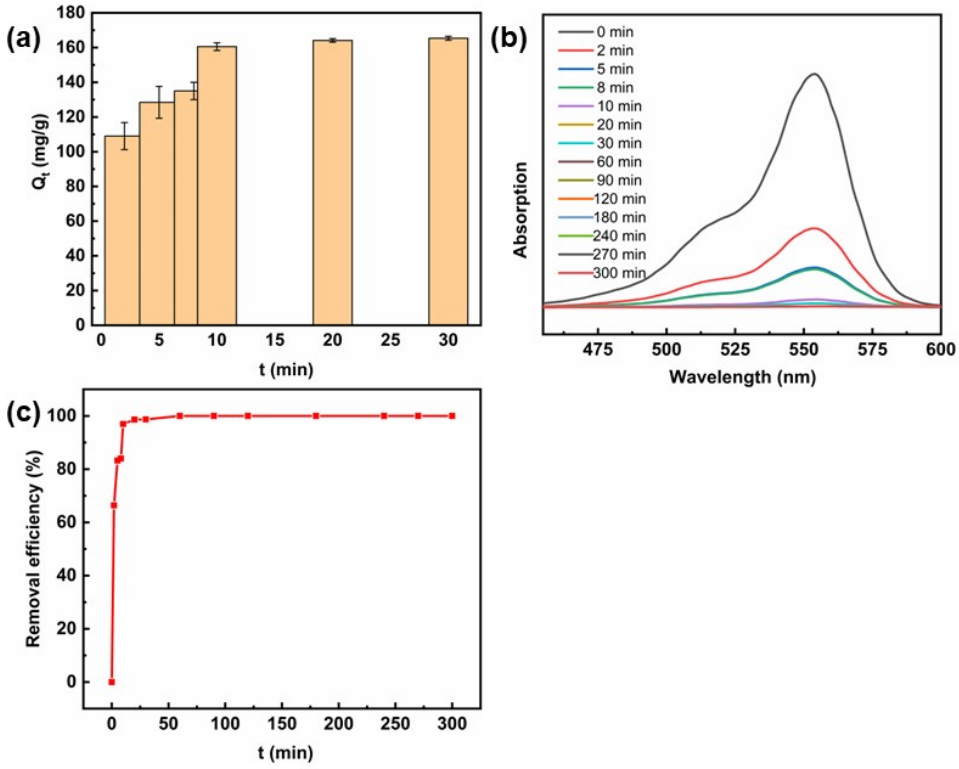

Fig. S8. The adsorption kinetics of BIPOP-1 towards RB. (a) Kinetic equilibrium curve of RB onto BIPOP-1 with an initial concentration of 50 mg/L with the error bars based on triplicate measurements. (b) The time-dependent UV-vis spectra along with time plot; (c) The removal efficiency (%) vs time plot.

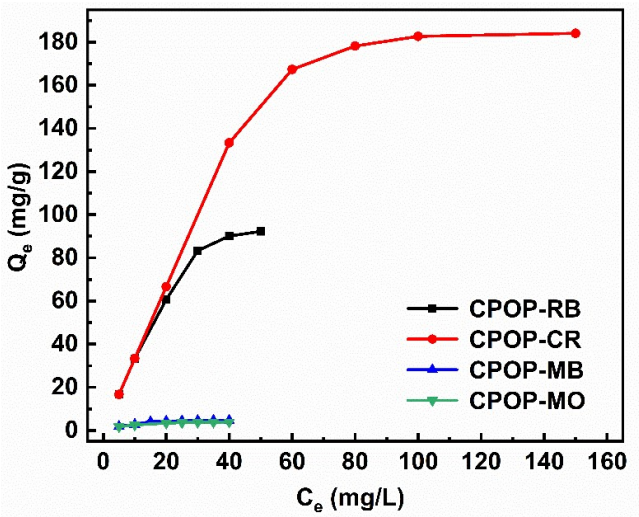

Fig. S9. Equilibrium adsorption isotherms of CPOP towards various dyes

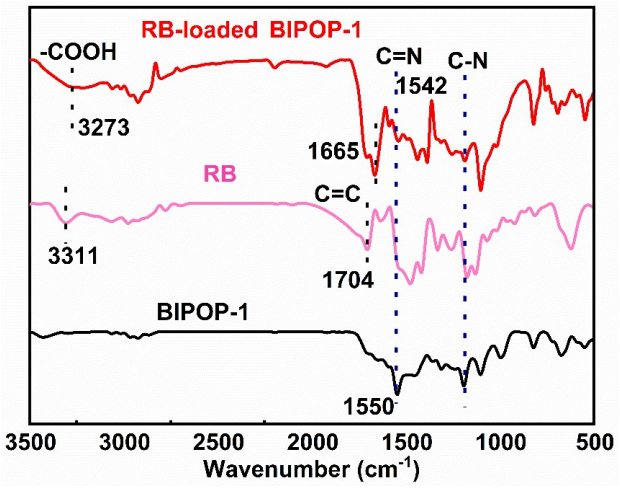

Fig. S10. FT-IR spectroscopy of BIPOP-1, RB and RB-loaded BIPOP-1

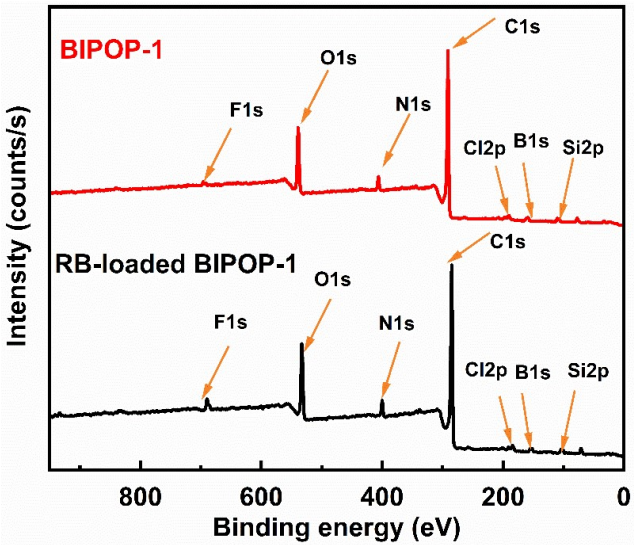

Fig. S11. Wide-scan XPS spectra of BIPOP-1 and RB-loaded BIPOP-1

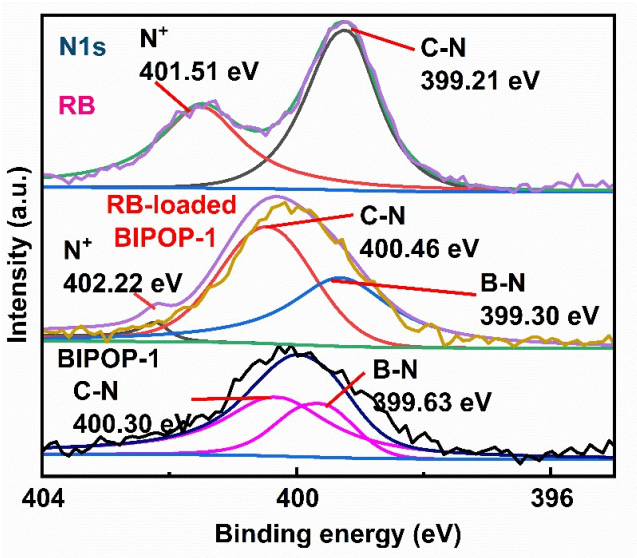

Fig. S12. High resolution XPS spectra of N1s

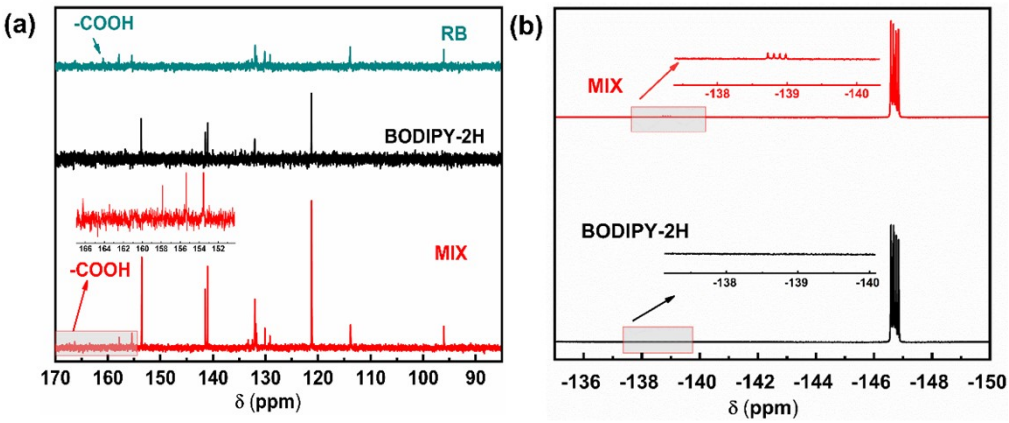

Fig. S13. (a) ^{13}C NMR spectra of RB, and BODIPY-2H, and their mixture; (b) ^{19}F NMR spectra of BODIPY-2H and its mixture with RB

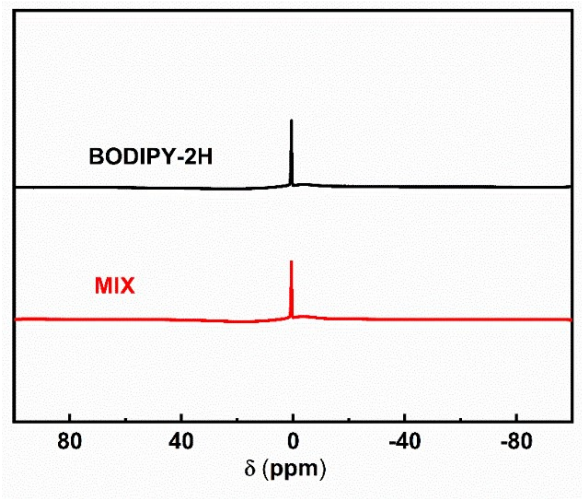

Fig. S14. The ^{11}B NMR spectra of BODIPY-2H and its mixture with RB

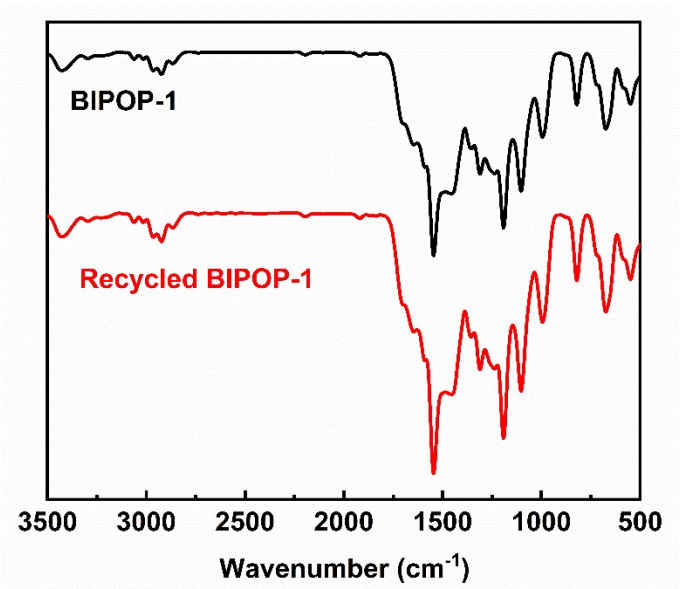

Fig. S15. The FT-IR spectroscopy of the pristine and recycled BIPOP-1

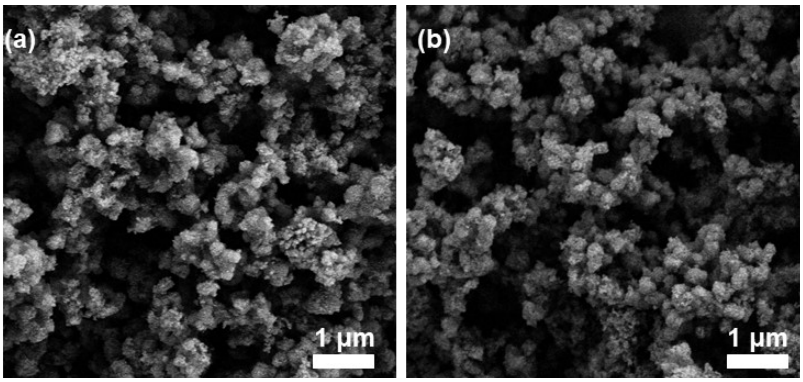

Fig. S16. The FE-SEM images of the pristine and recycled BIPOP-1

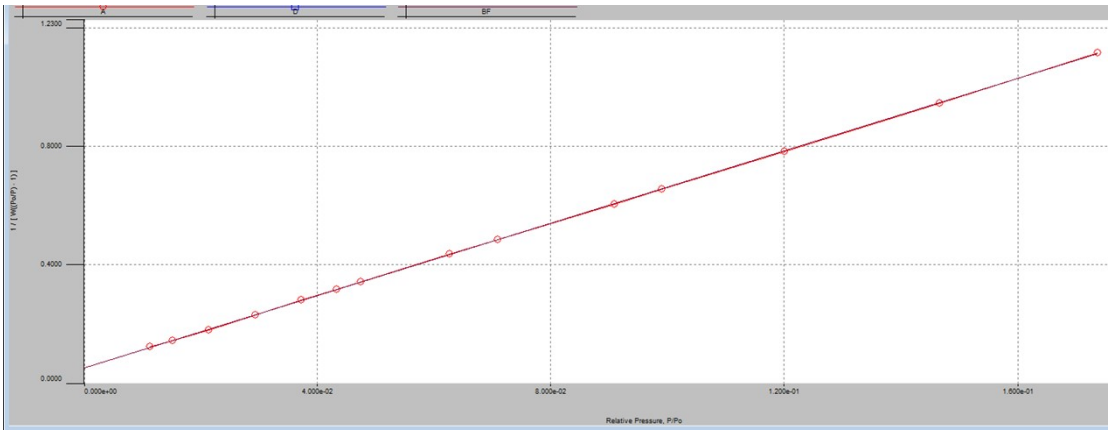

Fig. S17. BET plots of BIPOP-1 (r = 0.999982, C = 118.639)

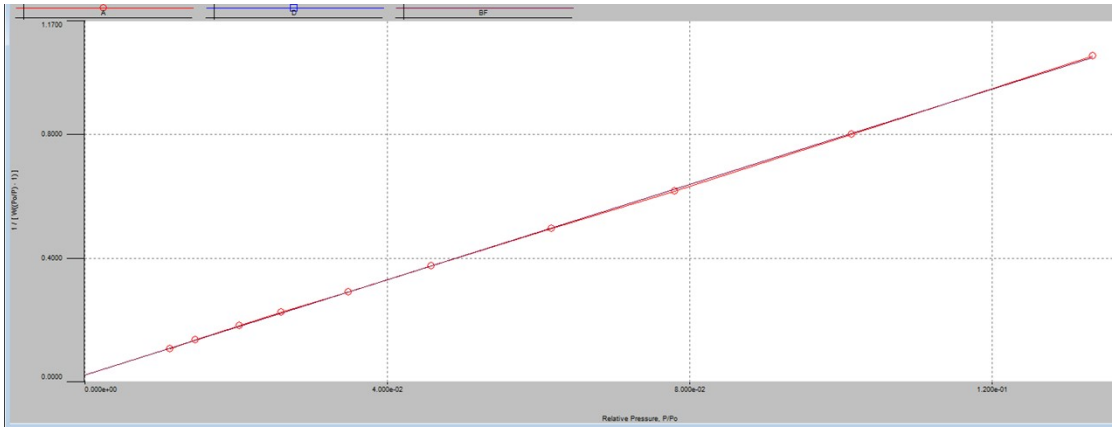

Fig. S18. BET plots of BIPOP-2 (r = 0.999947, C = 378.787)

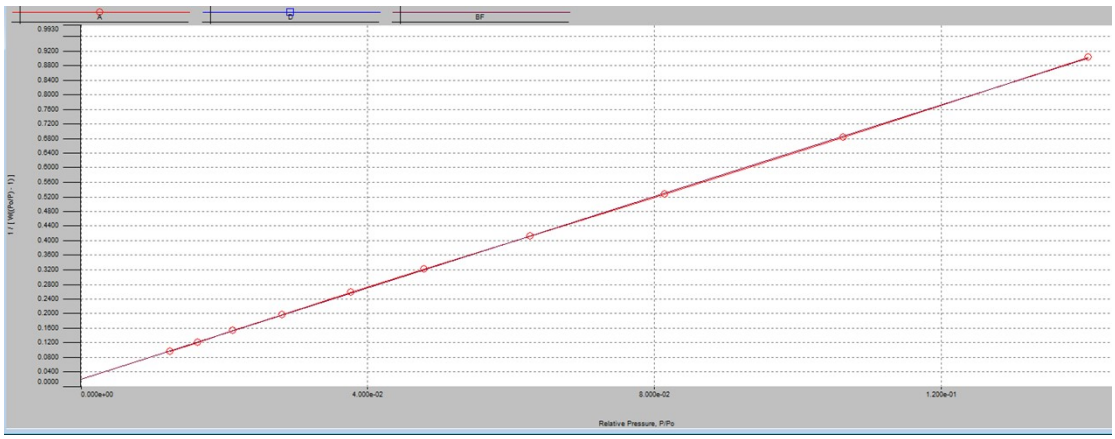

Fig. S19. BET plots of CPOP (r = 0.999977, C = 325.499)

Table S1. Comparison of the adsorption capacities of BIPOPs towards MO with other adsorbents

Adsorbents	**Adsorption Capacity /mg g^{-1}**	**Ref.**
BIPOP-1	211.8	**This work**
BIPOP-2	162.0	**This work**
Zeolitic imidazole frameworks	1340	1
amorphous carbon nanotubes	253.26	2
UiO-66-NH_2	242.72	3
activated carbon prepared from date pits	434	4
QPEI/SiO	105.4	5
SiO_2 nanofibers	730.9	6
rambutan-like $MnCo_2O_4$	185.14	7
Lignin derived ZSM-5 (PZ)	514	8

halloysite nanotubes/polypyrrole nanocomposites	214.6	9
chitosan/polyvinyl alcohol/zeolite electrospun composite nanofibrous membrane	153	10
copper-modified nanoalum	139	11
Modified nickel ferrite nanocomposite/functionalized chitosan	551.2	12
calcined Zn-Al layered double hydroxide	451.21	13
magnetic aminated lignosulfonate/carbon	121.28	14
Sensitized Bentonite	99.3	15
sugar beet bagasse	221.5	16
Cu_2O/Bi_2O_3	1533.2	17
Superparamagnetic nanosorbent	240	18
CTA-CSM	131.9	19

Table S2. Comparison of the adsorption capacity of BIPOPs on CR with other adsorbents

Adsorbents	**Adsorption Capacity /mg g^{-1}**	**Ref.**
BIPOP-1	1477.4	**This work**
BIPOP-2	1280.1	**This work**
Congo red dye	1735	20
Zeolitic imidazole frameworks	3900	1
Nano-Cao	357.14	21
biochar derived from leather shavings	1916	22
Cationic Lignin Hydrogels	125.63	23
amorphous carbon nanotubes	467.97	2
titanium dioxide	152	24
$FexCo_3$-xO_4 nanoparticles	128.6	25
Fe_3O_4@$nSiO_2$@$mSiO_2$	1428	26
fibrous xonotlite	574.71	27
Mg-Al-mixed metal oxide（MMO-E）	3470	28
Hierarchical porous Ni/Co-LDH hollow dodecahedron	909.2	29
Nano-Fe_3O_4	1395	30
Coconut husk-raw clay-Fe composite	1649.3	31

MOF-5/Cu	357.42	32
by coal-series kaolin	237.53	33
Zr-MOFs	1236.9	34

Table S3. Comparison of the adsorption capacity of BIPOPs on MB with other adsorbents

Adsorbents	**Adsorption Capacity /mg g^{-1}**	**Ref.**
BIPOP-1	287	**This work**
BIPOP-2	217	**This work**
activated carbon prepared from date pits	455	4
carbonaceous adsorbent	140.25	35
imprinted polymer	3628.84	36
porous soy protein isolate	272.4	37
Porous Biochar	208	38
activated carbon prepared from Malawian baobab fruit shell wastes	334.45	39
Chitosan crosslinked composite	499.8	40
biochar from solid wastes	161	41
$ZnCl_2$-activated carbon	255.1	42
AC-alginate composite membrane	666	43
Mesoporous-Activated Carbon	1000	44
dimensional titanate nanosheets	3937	45
slow pyrolysis pine cone bio-char	106.4	46
Treated digested residue	285.71	47
magnetic alginate/rice husk bio-composite	274.9	48
nanofibrous membranes	3186.7	49
Stomatocyte-like hollow polydopamine nanoparticles	2896	50

Table S4. Size and molecular properties of dye molecules

Dyes	Molecular Structure	Molecular Size (nm)	Molecular Weight (g/mol)	Nature	Adsorption wavelength (nm)
MB	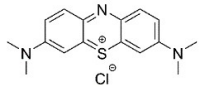	1.26*0.77*0.65	320	cationic	665
MO	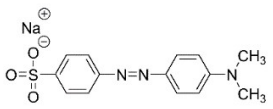	1.31*0.55*0.18	327	anionic	464

RB	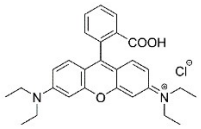	1.59*1.18*0.56	479	cationic	554
CR	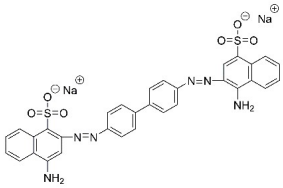	2.62*0.74*0.43	696	anionic	497

Table S5. The comparison of equilibrium adsorption capacities (Q_e) of RB adsorbed by BIPOP-1 in pure water and seawater from Bohai sea

	initial dye concentration (mg/L)	Q_e (mg g^{-1})
pure water	50	167
	500	1633
	1000	2207
seawater from Bohai sea	50	167
	500	1581
	1000	2191

Table S6. Electronic binding energy of various elements in BIPOP-1, RB, and RB-loaded BIPOP-1

		BIPOP-1	RB-loaded BIPOP-1	RB
B1s / eV	B-F	192.74	193.17	
	B-N	190.63	190.84	
F1s / eV	C-F	689.63	689.63	
	B-F	685.89	685.50	
Cl2p / eV	Cl^-		200.40	196.87
O1s / eV	C-O		533.45	533.48
	O-C=O		531.66	532.08
N1s / eV	C-N	400.30	400.46	399.21
	B-N	399.63	399.30	
	N^+		402.22	401.51

References

1. Zhang, Z.-h.; Zhang, J.-l.; Liu, J.-m.; Xiong, Z.-h.; Chen, X., Selective and competitive adsorption of azo dyes on the metal–organic framework ZIF-67. *Water, Air, & Soil Pollut.* **2016,** *227*, 1-12.

2. Zhong, L.; Tang, A.; Yan, P.; Wang, J.; Wang, Q.; Wen, X.; Cui, Y., Palygorskite-template amorphous carbon nanotubes as a superior adsorbent for removal of dyes from aqueous solutions. *J. Colloid Interface Sci.* **2019,** *537*, 450-457.

3. Liu, Q.; Zang, G.-L.; Zhao, Q., Removal of methyl orange wastewater by Ugi multicomponent reaction functionalized UiO-66-NS. *Environ. Sci. Pollut. Res.* **2022,** *29*, 76833-76846.

4. Mahmoudi, K.; Hosni, K.; Hamdi, N.; Srasra, E., Kinetics and equilibrium studies on removal of methylene blue and methyl orange by adsorption onto activated carbon prepared from date pits-A comparative study. *Korean J. Chem. Eng.* **2015,** *32* (2), 274-283.

5. Liu, J.; Ma, S.; Zang, L., Preparation and characterization of ammonium-functionalized silica nanoparticle as a new adsorbent to remove methyl orange from aqueous solution. *Appl. Surf. Sci.* **2013,** *265*, 393-398.

6. Batool, S.; Imran, Z.; Hassan, S.; Rasool, K.; Ahmad, M.; Rafiq, M., Enhanced adsorptive removal of toxic dyes using SiO_2 nanofibers. *Solid State Sci.* **2016,** *55*, 13-20.

7. Wang, K.; Wu, X.; Wu, W.; Chen, W.; Qin, L.; Cui, X., Synthesis of rambutan-like $MnCo_2O_4$ and its adsorption performance for methyl orange. *J. Therm. Anal. Calorim.* **2015,** *122*, 653-663.

8. Saini, K.; Sahoo, A.; Biswas, B.; Kumar, A.; Bhaskar, T., Preparation and characterization of lignin-derived hard templated carbon (s): Statistical optimization and methyl orange adsorption isotherm studies. *Bioresour. Technol.* **2021,** *342*, 125924.

9. Zhang, M.; Chang, L.; Yu, Z., Fabrication of halloysite nanotubes/polypyrrole nanocomposites for efficient removal of methyl orange. *Desalination and Water Treatment* **2018,** *110*, 209-218.

10. Habiba, U.; Siddique, T. A.; Lee, J. J. L.; Joo, T. C.; Ang, B. C.; Afifi, A. M., Adsorption study of methyl orange by chitosan/polyvinyl alcohol/zeolite electrospun composite nanofibrous membrane. *Carbohydr. Polym.* **2018,** *191*, 79-85.

11. He, Y.; Li, H.; Zhou, L.; Xu, T.; Peng, C.; Liu, H., Removal of methyl orange from aqueous solutions by a novel hyper-cross-linked aromatic triazine porous polymer. *Acta Phys.-Chim. Sin* **2019,** *35*, 299-306.

12. Moghaddam, A. Z.; Ghiamati, E.; Pourashuri, A.; Allahresani, A., Modified nickel ferrite nanocomposite/functionalized chitosan as a novel adsorbent for the removal of acidic dyes. *Int. J. Biol. Macromol.* **2018,** *120*, 1714-1725.

13. Djezar, H.; Rida, K.; Salhi, M., Efficient adsorbent for the removal of methyl orange and Congo red by calcined Zn-Al layered double hydroxide. *Inorg. Nano-Metal Chem.* **2022,** *52*, 161-172.

14. Borsalani, H.; Nikzad, M.; Ghoreyshi, A. A., Extraction of lignosulfonate from black liquor into construction of a magnetic lignosulfonate-based adsorbent and its adsorption properties for dyes from aqueous solutions. *J. Polym. Environ.* **2022,** *30*, 4068-4085.

15. Mutahir, S.; Irfan, T.; Nadeem, N.; Humayun, M.; Khan, M. A.; Refat, M. S.; Wang, C.; Sheikh, T. A., Synthesis and Micromechanistic Studies of Sensitized Bentonite for Methyl Orange and Rhodamine-B Adsorption from Wastewater: Experimental and DFT-Based Analysis. *Molecules* **2022,** *27*, 5567.

16. Ghorbani, F.; Kamari, S., Application of response surface methodology for optimization of methyl orange adsorption by Fe-grafting sugar beet bagasse. *Adsorp. Sci. Technol.* **2017,** *35* (3-4), 317-338.

17. Tang, H.; Yang, W.; Fu, L.; Zhu, J.; Li, D.; Zhou, L., Excellent adsorption capacity and photocatalytic regeneration of nanoparticles-assembled mesoporous Cu_2O/Bi_2O_3 composites for removal of methyl orange. *Mater. Res. Exp.* **2019,** *6*, 085532.

18. Gallo-Cordova, A.; Lemus, J.; Palomares, F. J.; Morales, M.; Mazarío, E., Superparamagnetic nanosorbent for water purification: Assessment of the adsorptive removal of lead and methyl orange from aqueous solutions. *Sci. Total Environ.* **2020,** *711*, 134644.

19. Ke, P.; Zeng, D.; Xu, K.; Cui, J.; Li, X.; Wang, G., Preparation of quaternary ammonium salt-modified chitosan microspheres and their application in dyeing wastewater treatment. *ACS omega* **2020,** *5*, 24700-24707.

20. Kim, S.-H.; Choi, P.-P., Enhanced Congo red dye removal from aqueous solutions using iron nanoparticles: adsorption, kinetics, and equilibrium studies. *Dalton Transactions* **2017,** *46*, 15470-15479.

21. Xia, H.; Chen, L.; Fang, Y., Highly efficient removal of Congo red from wastewater by nano-cao. *Sep. Sci. Technol.* **2013,** *48*, 2681-2687.

22. Huang, X.; Yu, F.; Peng, Q.; Huang, Y., Superb Adsorption Capacity of Biochar Derived from Leather Shavings for Congo.

23. Wang, C.; Feng, X.; Li, W.; Shang, S.; Zhang, H., Fabricating Cationic Lignin Hydrogels for Dye Adsorption. *J. Renew. Mater.* **2023,** *11*, 1793-1805.

24. Abbas, M., Experimental investigation of titanium dioxide as an adsorbent for

removal of Congo red from aqueous solution, equilibrium and kinetics modeling. *J. Water Reuse Desal.* **2020,** *10*, 251-266.

25. Liu, J.; Wang, N.; Zhang, H.; Baeyens, J., Adsorption of Congo red dye on $Fe_xCo_{3-x}O_4$ nanoparticles. *J. Environ. Manag.* **2019,** *238*, 473-483.

26. Zhang, Y.; Bai, L.; Zhou, W.; Lu, R.; Gao, H.; Zhang, S., Superior adsorption capacity of Fe_3O_4@ $nSiO_2$@ $mSiO_2$ core-shell microspheres for removal of congo red from aqueous solution. *J. Mol. Liq.* **2016,** *219*, 88-94.

27. Han, M.; Shen, X.; Shao, H.; Wang, X.; Liu, Y.; Zhai, Y., Adsorption of Congo red by fibrous xonotlite prepared from waste silicon residue. *Water Sci. Technol.* **2022,** *85*, 3159-3168.

28. Xie, J.; Yamaguchi, T.; Oh, J.-M., Synthesis of a mesoporous Mg–Al–mixed metal oxide with P123 template for effective removal of Congo red via aggregation-driven adsorption. *J. Solid State Chem.* **2021,** *293*, 121758.

29. Hu, H.; Liu, J.; Xu, Z.; Zhang, L.; Cheng, B.; Ho, W., Hierarchical porous Ni/Co-LDH hollow dodecahedron with excellent adsorption property for Congo red and Cr (VI) ions. *Appl. Surf. Sci.* **2019,** *478*, 981-990.

30. Tang, Z. X.; Chen, Y.; Xue, J.; Yue, S. In Adsorption and removal of Congo red dye from aqueous solution by using nano-Fe_3O_4, *Adv. Mater. Res.* **2012**, *503-504*, 262-265.

31. Adebayo, M. A.; Jabar, J. M.; Amoko, J. S.; Openiyi, E. O.; Shodiya, O. O., Coconut husk-raw clay-Fe composite: preparation, characteristics and mechanisms of Congo red adsorption. *Sci. Rep.* **2022,** *12*, 14370.

32. Mosavi, S. H.; Zare-Dorabei, R.; Bereyhi, M., Rapid and Effective Ultrasonic-Assisted Adsorptive Removal of Congo Red onto MOF-5 Modified by CuCl2 in Ambient Conditions: Adsorption Isotherms and Kinetics Studies. *ChemistrySelect* **2021,** *6*, 4432-4439.

33. Niu, S.; Xie, X.; Wang, Z.; Zheng, L.; Gao, F.; Miao, Y., Enhanced removal performance for Congo red by coal-series kaolin with acid treatment. *Environ. Technol.* **2021,** *42*, 1472-1481.

34. Yang, Q.; Wang, Y.; Wang, J.; Liu, F.; Hu, N.; Pei, H.; Yang, W.; Li, Z.; Suo, Y.; Wang, J., High effective adsorption/removal of illegal food dyes from contaminated aqueous solution by Zr-MOFs (UiO-67). *Food Chem.* **2018,** *254*, 241-248.

35. Wang, Y.; Zhou, Y.; Jiang, G.; Chen, P.; Chen, Z., One-step fabrication of carbonaceous adsorbent from corncob for enhancing adsorption capability of

methylene blue removal. *Sci. Rep.* **2020,** *10*, 12515.
36. Wang, N.; Xiao, S.-J.; Su, C.-W., Preparation of molecularly imprinted polymer for methylene blue and study on its molecular recognition mechanism. *Colloid. Polym. Sci.* **2016,** *294*, 1305-1314.
37. Liu, F.; Zou, H.; Hu, J.; Liu, H.; Peng, J.; Chen, Y.; Lu, F.; Huo, Y., Fast removal of methylene blue from aqueous solution using porous soy protein isolate based composite beads. *Chem. Eng. J.* **2016,** *287*, 410-418.
38. Han, X.; Chu, L.; Liu, S.; Chen, T.; Ding, C.; Yan, J.; Cui, L.; Quan, G., Removal of methylene blue from aqueous solution using porous biochar obtained by KOH activation of peanut shell biochar. *BioResources* **2015,** *10*, 2836-2849.
39. Vunain, E.; Biswick, T., Adsorptive removal of methylene blue from aqueous solution on activated carbon prepared from Malawian baobab fruit shell wastes: Equilibrium, kinetics and thermodynamic studies. *Sep. Sci. Technol.* **2019,** *54*, 27-41.
40. Liu, X.-J.; Li, M.-F.; Ma, J.-F.; Bian, J.; Peng, F., Chitosan crosslinked composite based on corncob lignin biochar to adsorb methylene blue: Kinetics, isotherm, and thermodynamics. *Colloid Surface A* **2022,** *642*, 128621.
41. Franciski, M. A.; Peres, E. C.; Godinho, M.; Perondi, D.; Foletto, E. L.; Collazzo, G. C.; Dotto, G. L., Development of CO_2 activated biochar from solid wastes of a beer industry and its application for methylene blue adsorption. *Waste Manage.* **2018,** *78*, 630-638.
42. Li, Y.; Li, Y.; Zang, H.; Chen, L.; Meng, Z.; Li, H.; Ci, L.; Du, Q.; Wang, D.; Wang, C., ZnCl2-activated carbon from soybean dregs as a high efficiency adsorbent for cationic dye removal: isotherm, kinetic, and thermodynamic studies. *Environ. Technol.* **2020,** *41*, 2013-2023.
43. Durrani, W. Z.; Nasrullah, A.; Khan, A. S.; Fagieh, T. M.; Bakhsh, E. M.; Akhtar, K.; Khan, S. B.; Din, I. U.; Khan, M. A.; Bokhari, A., Adsorption efficiency of date palm based activated carbon-alginate membrane for methylene blue. *Chemosphere* **2022,** *302*, 134793.
44. Lawtae, P.; Tangsathitkulchai, C., The use of high surface area mesoporous-activated carbon from longan seed biomass for increasing capacity and kinetics of methylene blue adsorption from aqueous solution. *Molecules* **2021,** *26* (21), 6521.
45. Yuan, H.; Ma, S.; Wang, X.; Long, H.; Zhao, X.; Yang, D.; Lo, W. H.; Tsang, Y. H., Ultra-high adsorption of cationic methylene blue on two dimensional titanate nanosheets. *RSC Adv.* **2019,** *9*, 5891-5894.

46. Dawood, S.; Sen, T. K.; Phan, C., Synthesis and characterization of slow pyrolysis pine cone bio-char in the removal of organic and inorganic pollutants from aqueous solution by adsorption: kinetic, equilibrium, mechanism and thermodynamic. *Bioresour. Technol.* **2017,** *246*, 76-81.
47. Anfar, Z.; El Haouti, R.; Lhanafi, S.; Benafqir, M.; Azougarh, Y.; El Alem, N., Treated digested residue during anaerobic co-digestion of Agri-food organic waste: methylene blue adsorption, mechanism and CCD-RSM design. *J. Environ. Chem. Eng.* **2017,** *5* (6), 5857-5867.
48. Alver, E.; Metin, A. Ü.; Brouers, F., Methylene blue adsorption on magnetic alginate/rice husk bio-composite. *Int. J. Biol. Macromol.* **2020,** *154*, 104-113.
49. Gao, T.; Guan, G.; Wang, X.; Lou, T., Electrospun molecularly imprinted sodium alginate/polyethylene oxide nanofibrous membranes for selective adsorption of methylene blue. *Int. J. Biol. Macromol.* **2022,** *207*, 62-71.
50. Lin, J.; Wang, H.; Ren, E.; Song, Q.; Lan, J.; Chen, S.; Yan, B., Stomatocyte-like hollow polydopamine nanoparticles for rapid removal of water-soluble dyes from water. *Chem. Commun.* **2019,** *55*, 8162-8165.